

An Investigation into the Effect of Hydrotalcite Calcination Temperature on the Catalytic Performance of Mesoporous Ni-MgO-Al₂O₃ Catalyst in the Combined Steam and Dry Reforming of Methane

Gholamreza Roohollahi¹ and Mohammadreza Ehsani^{2*}

¹ R&D Manager, Kharazmi Technology Development Company, Tehran, Iran

² Professor, Department of Chemical Engineering, Isfahan University of Technology, Isfahan, Iran

Received: May 16, 2018; revised: September 03, 2018; accepted: September 12, 2018

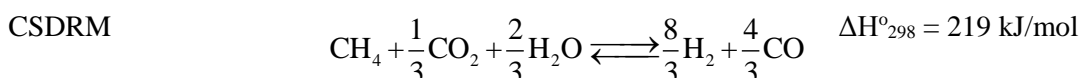
Abstract

Several mesoporous nickel-based catalysts with MgO-Al₂O₃ as the catalyst support were prepared using a co-precipitation method at a constant pH. The supports were prepared from the decomposition of an Mg-Al hydrotalcite-like structure which had already been prepared with Mg/Al=1. Prior to impregnating 10 wt.% nickel on the supports, the precursor was decomposed at several temperatures of 500, 600, 700, and 800 °C in order to elucidate the effect of calcination temperature on the physical and chemical characteristics of Mg-Al mixed oxides and the ultimate catalytic performance of the synthesized catalysts in the combined steam and dry reforming (CSDRM). The catalyst the precursor of which was calcined at 700 °C shows an excellent nickel dispersion and the highest activity among the other samples. It also exhibits the most stable performance during the long-term 36-hour run with high resistance against coke formation in the harsh condition of CSDRM.

Keywords: Combined Steam and Dry Reforming, MgO-Al₂O₃, Mesoporous, Hydrotalcite-derived Catalysts

1. Introduction

Nowadays, synthesis gases (syngas) as the vital source of petrochemical products are produced mainly through the reforming reaction of hydrocarbons, especially natural gas over heterogeneous catalysts (Rostrup-Nielsen et al., 2002). Among different technologies which are established or developing for the generation of the syngas, combined steam and dry reforming of methane (CSDRM) as an attractive CO₂ valorization route and a safe process yields a syngas with an H₂/CO molar ratio close to 2 to meet the requirements of the plants of direct reduction of iron (DRI) using syngas (Park et al., 2015), methanol production (Olah et al., 2011, 2012, 2015), and DME and Fisher-Tropsch processes (Song et al., 2006; Koo et al., 2008; Rostrup-Nielsen et al., 2011). Compared to methane dry reforming, the merits of such a reaction are being less endothermic and obtaining an adjustable H₂/CO ratio by varying the composition of oxidants, CO₂, and H₂O in the reactor feedstock.



* Corresponding author:
Email: Ehsanimr@cc.iut.ac.ir



In recent years, many researchers have studied the CSDRM over catalysts containing both noble or transition metals (Olah et al., 2011; Bae et al., 2011; Rong et al. 2017; Itkulova et al., 2018; Son et al., 2013; Mehr et al., 2002; Siang et al., 2018; Danilova et al., 2015; Yang et al., 2018; Roh et al., 2007, 2008, 2009; Koo et al., 2009, 2012, 2014; Jabbour et al., 2015, 2016; Huang et al., 2008). Although nickel is an active and selective metal for being utilized in the CSDRM reaction and is significantly less expensive and more available rather than noble metals, the main drawbacks of this economic selection are rapid sintering and a relatively high tendency to carbon formation under the harsh conditions of CSDRM reaction, which leads to the rapid deactivation of the catalyst (a low steam/carbon ratio and a high CO_2 content) (Jabbour et al., 2016). Therefore, in order to enhance the catalyst stability, it is necessary to prepare catalysts with lower potential for carbon deposition and a lower sintering rate of nickel particles.

Numerous studies demonstrate that a proper way of reducing the sintering rate of nickel particles is improving the metal-carrier/support interaction, which in turn retards the nickel particle coarsening and enhances the catalyst stability (Koo et al., 2008; Sehested et al. 2006; Christensen et al. 2006). Catalysts based on MgO supports show high stability since the strong interaction between nickel particles and carrier decreases the sintering rate of the active metal. In addition, owing to the higher basicity compared to aluminum oxide, calcium aluminate and magnesium aluminate spinels result in lower coke formation (Koo et al., 2008; Mehr et al. 2002; Koo et al. 2009). However, MgO carrier generally has a higher nickel crystallite size and a lower nickel dispersion due to the lower surface area of the synthesized carrier. It should be noted that smaller Ni particles induce the carbon removal by CO_2 and H_2O more rapidly. The experimental results indicate a strong correlation between the nickel crystal size and the resistance to carbon formation (Christensen et al. 2006; Zhang et al., 2013).

Among the numerous efforts made during the development of more proper catalyst carriers for CSDRM, Mg-Al mixed oxides derived from hydrotalcite-like materials exhibited a higher activity and stability in CSDRM due to the enhanced steam and CO_2 adsorption, basic property, fine dispersion, and strong Ni to support interaction (Koo et al., 2009; Roh et al. 2007; Jabbour et al., 2017). These catalysts can be synthesized using different preparation methods like the impregnation of pre-calcined carriers or the simultaneous co-precipitation of the mostly nitrate-based solution of all the constituents.

Mg-Al hydrotalcite-like components with the general formula of $[\text{Mg}^{II}_{1-x}\text{Al}^{III}_x(\text{OH})_2]^{x+}(\text{CO}_3^{2-})_{x/2} \cdot m\text{H}_2\text{O}$ could be a proper candidate for the precursor used in the preparation of a thermally stable mesoporous MgO- Al_2O_3 carrier with a high surface area (Fonseca et al., 2005). The thermal decomposition of Mg-Al hydrotalcite-like (HT-like) component produces a well dispersed mixture of magnesium and aluminum oxides (Xu et al., 2011). In a study conducted by Di Cosimo et al., the effect of Mg/Al ratio on the surface area, crystallite size, and the density and type of basic sites of different HT-like materials was investigated. It was shown that the highest surface area, the highest density of the basic sites, and the smallest crystallite sites of the catalyst carrier were obtained at Mg/Al=1 (Koo et al., 2009). In another research conducted by Koo et al., the effect of Mg/Al ratio was explored. In their study, they concluded that the minimum coke content after stability test was obtained for the sample with Mg/Al=0.5. Despite the higher basicity of the samples with higher Mg/Al, the surface area of the catalyst support and the surface area of active metal nickel may be considerably reduced. However, such a conclusion was inferred from the Mg/Al ratio of 0.5, 1.3, and 3.5, while the HT calcination temperature was 800 °C for all the carriers (Koo et al., 2009).

Apart from Mg/Al ratio, many other synthesis parameters, including the way of performing co-precipitation (preparation at high or low supersaturation) and calcination temperature can be influential on the properties of the final mixed oxide (Cavani et al., 1991; Sato et al., 1986; Arizaga et al. 2007). Compared to high supersaturation conditions, co-precipitation at low supersaturation at a constant pH (pH control during synthesis) gives rise to higher crystalline material with a relatively smaller particle size, so it may yield a material with a higher surface area (Duan et al., 2006).

The catalyst activity, stability, and resistance to coke deposition can be notably influenced by the particle size of active metal Ni, the extents of metal–support interaction, the surface basicity of the catalyst, and the promotion efficiency of Mg promoter. These determining parameters, by themselves, can be affected by varying the calcination temperature during the preparation process. On the other side, the amount of the inactive spinel phase formed generally increases by raising calcination temperature; therefore, great care should be taken to keep the calcination temperature as low as possible (Tan et al., 2015; Seo et al., 2010; Boukha et al., 2010; Schulze et al., 2001). Ramasamy et al. showed that the calcination temperature had a minimal effect on the physical properties but a remarkable influence on the type and density of the basic properties (Ramasamy et al., 2016). Daza et al. also performed dry reforming on HT calcined at different temperatures and observed the highest activity at 700 °C (Daza et al., 2012). In a study published by Christensen et al., the collapse of the support along with the growth rate of nickel particle size during the sintering experiments confirmed that the sample with MgO/Al₂O₃=50/50 (wt.% basis) had the least growth rate but the highest stability among other hydrotalcite samples with no detection of inactive nickel aluminate spinel. Koo et al. investigated the metal-support interaction (MSI) in the CSDRM using Ni catalysts supported on MgO-Al₂O₃ which was derived from the decomposition of Mg-Al hydrotalcite. They reported that the pre-calcination temperature (in the range of 800-1200 °C) of hydrotalcite (containing 29 wt.% MgO) had a significant influence on MSI and subsequently on the catalyst performance. It was concluded that the precursor pre-calcined at the lowest temperature, i.e. 800 °C, had the strongest MSI, the smallest nickel crystallite size, the highest catalytic activity, and the highest resistance against coke formation (Koo et al., 2008).

This contribution aims to elucidate the effect of HT calcination temperature on the characteristics of the final catalyst and its catalytic behavior in the CSDRM reaction.

2. Experimental

2.1. Support preparation

The Mg-Al hydrotalcite (HT) precursors with the general formula of $[M(II)_{1-x}M(III)_y(OH)_2](CO_3)_{x/2}nH_2O$, where M(II) = Mg and M(III) = Al, have been prepared using the co-precipitation method at low supersaturation. A series of Mg–Al HT-like precursors with different Mg/Al molar ratios was prepared using the co-precipitation method at a constant pH of 10.0±0.05 and a temperature of 60 °C. 1.5 M aqueous solutions of the magnesium nitrates and aluminum nitrates, which were prepared from 99% magnesium hexahydrate and 98.5% aluminum nonahydrate from Merck Company respectively, were prepared separately mixed together. The precipitating agent was a mixture of 1.5 M Na₂CO₃ and 2.0 M NaOH. The precipitation was then carried out by simultaneously adding the mixed metal solution and the precipitating agents into a jacketed glass reactor initially filled by 500 ml deionized water. The temperature of the precipitating liquid was accurately controlled using a water circulating jacket with the least fluctuation (within ±0.5 °C). An accurate pH controller was utilized in order to automatically control the acidity of the solution during the addition of both nitrate and alkaline solutions. The precipitates formed were aged in the mother liquor for different times and then recovered by filtration. In order to avoid any bias during the catalyst characterization and catalyst performance

testing through the remaining sodium content, the precipitates were thoroughly washed three times with warm deionized water until the sodium content reached less than 0.01 wt.% (based on the atomic absorption spectroscopy analysis). The precursors dried at 100 °C overnight and calcined at different temperatures for 4 hours in order to obtain the mixed oxides.

2.2. Catalyst preparation

The calcined HT-like components were impregnated with nickel nitrate solution (99% nickel nitrate hexahydrate, from Merck Company) using the incipient wetness impregnation technique to obtain a catalyst containing fixed 10wt.% nickel. The impregnated samples were first dried at 120 °C for 10 hours, subsequently heated at a rate of 5 °C/min up to 600 °C, and finally maintained at 600 °C for 4 hours.

2.3. Characterization of the precursors and catalysts

The chemical composition of the samples was determined using a Varian 240FS flame atomic absorption spectroscope. The specific surface area of the samples was measured using nitrogen adsorption at 77 K using a Micromeritics TRISTAR II Plus 3030 and BET analysis methods. The pore volume of the samples was determined at ($P/P_0=0.995$) obtained from N_2 isotherms. The pore size distributions of the samples were also calculated using BJH method. Prior to the test, the samples were degassed at 300 °C for 4 hrs. Powder X-ray power diffraction (XRD) patterns were recorded by X-ray diffraction (PANalytical Philips PW1730X) at a scanning rate of 2 °/min from 10° to 80° operating at 40 kV and 30 mA by using $CuK_{\alpha 1}$ radiation ($\lambda = 1.54060 \text{ \AA}$ 40 kV and 30 mA). The crystalline size of the HT, magnesium oxide, and Ni species was calculated according to the Scherrer Equation:

$$d = \frac{K \lambda}{\beta \cos \theta} \quad (1)$$

where, d is the mean size of species, and K is a dimensionless shape factor (assumed here to be 0.9); λ also stands for the X-ray wavelength, and β represents the line broadening at half of the maximum intensity, full width at half maximum (FWHM), in radian; θ also is the scattering angle in degrees and half of the Bragg angle (Cullity et al., 2013).

The dispersion, metal surface area, and particle size of metallic nickel particles were measured by H_2 pulse chemisorption method using Belsorp-MAX equipment. The dispersion, surface area, and mean particle size of nickel were evaluated according to following equations:

$$D_m = \frac{V_{chem} \times S.F. \times M.W.}{W/100} \times 100 \quad (2)$$

$$N.SA = V_{chem} \times N_{Av} \times S.F. \times a_{Ni} \quad (3)$$

$$d_{av} = \frac{6 \times W}{N.SA \times N_{Av} \times \rho} \times 10 \quad (4)$$

where, D_m is nickel dispersion (%), and V_{chem} is the chemisorbed volume (mol/g). S.F., M.W. (g/gmol), and N.SA (m^2/g) represent stoichiometric factor (for hydrogen chemisorption, H/Ni=1), nickel molecular weight equal to 58.69 (g/gmol), and nickel surface area respectively. N_{Av} is Avogadro Number equal to 6.023×10^{23} (atoms/gmol), and a_{Ni} denotes nickel cross section equal to 6.49×10^{-20}

(m^2/Ni atoms); ρ is also nickel density equal to 8.908 g/cm^3 , and d_{av} stands for average nickel crystallite diameter (nm) (Marquevich et al., 2003; Yaakob et al., 2013).

Temperature programmed reduction (TPR) was performed using the same device as mentioned for chemisorption analysis to identify the reduction temperature and the hydrogen consumption of the catalysts. A sample of 0.1 g was degassed with a 50 mL/min helium gas at $250 \text{ }^\circ\text{C}$ for 4 hrs, then cooled down to $50 \text{ }^\circ\text{C}$, and finally re-heated by an electrical furnace at a heating rate of $20 \text{ }^\circ\text{C}/\text{min}$ from 100 to $1000 \text{ }^\circ\text{C}$ under 10% H_2 in Argon gas.

The FT-IR spectra were recorded on a JASCO 4200 spectrometer using KBr discs, and the sample peaks in the wavelength range of $4000\text{-}400 \text{ cm}^{-1}$ were analyzed.

The total carbon analysis was performed using a Thermo Quest, Flash EA 1112 to measure the amount of coke deposited over the catalyst samples.

2.4. Catalyst performance testing

The CSDRM reaction was carried out in a fixed-bed SS310 reactor with an inside diameter of 12 mm equipped with a long thermowell having an outside diameter of 4-mm at atmospheric pressure. A schematic representation of the catalyst evaluation unit is displayed in Figure 1.

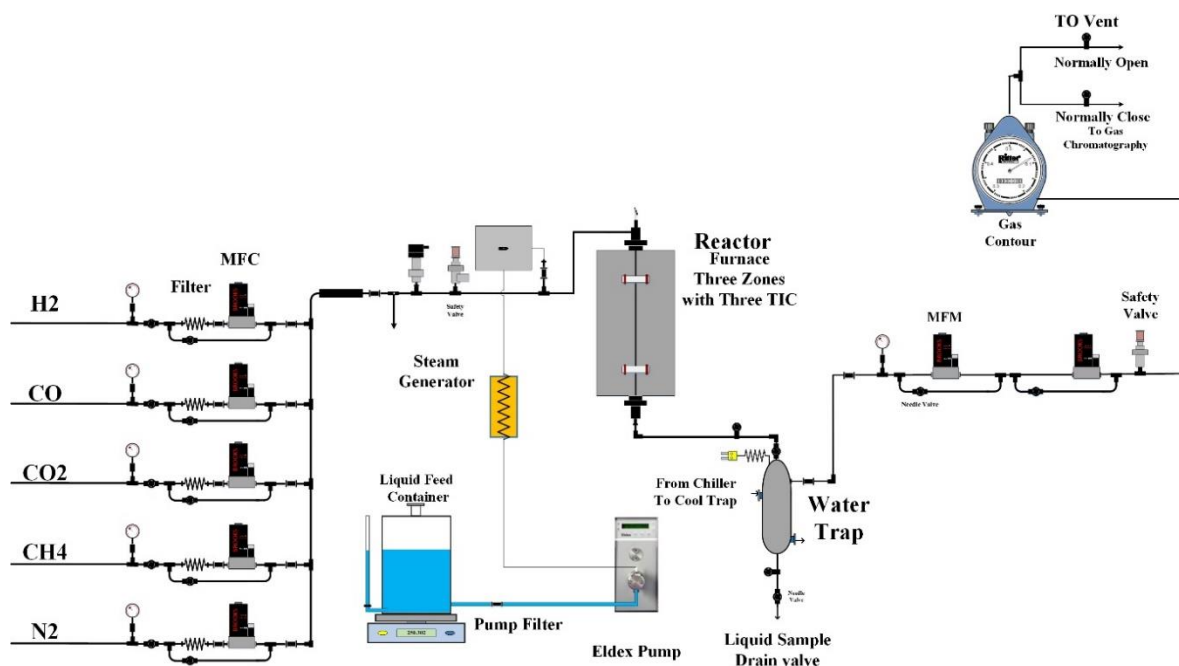


Figure 1

A schematic representation of the catalyst evaluation unit.

The reactor was placed inside an electrical furnace with three thermally independent zones. About 100 mg of the catalyst was crushed, sieved, and diluted with 1000 mg tabular alumina with the same size in order to provide an isothermal operation. The diluted bed was charged in the middle of the reactor while two inert tabular alumina beds were at the top and bottom of the catalyst bed. The reaction temperature was controlled by a K-type thermocouple inserted into the reactor thermowell adjacent to the catalyst bed. According to the desired feed composition, pure grade (purity of 99.999%) gases were mixed together. Liquid deionized water was dosed accurately using an Eldex 1SMP pump and vaporized into

a steam generator in order to be injected into the mixed gas stream. The water content from the reactor effluent was first trapped and the dried gas was directly sent to Agilent 7890A RGA, equipped with two thermal conductivity detectors and one flame ionization detector series having an appropriate packed and capillary column in order to separate permanent gases.

The conversions of methane and carbon dioxide were calculated by the following equations:

$$\text{CH}_4 \text{ Conversion}(\%) = \frac{F_{\text{CH}_4 \text{ in}} - F_{\text{CH}_4 \text{ out}}}{F_{\text{CH}_4 \text{ in}}} \times 100 \quad (5)$$

$$\text{CO}_2 \text{ Conversion}(\%) = \frac{F_{\text{CO}_2 \text{ in}} - F_{\text{CO}_2 \text{ out}}}{F_{\text{CO}_2 \text{ in}}} \times 100 \quad (6)$$

where, $F_{\text{CH}_4, \text{in}}$, $F_{\text{CH}_4, \text{out}}$, $F_{\text{CO}_2, \text{in}}$, and $F_{\text{CO}_2, \text{out}}$ stand for the molar flowrate of CH_4 and CO_2 at the inlet and outlet respectively.

The CSDRM was performed at a space velocity of 150,000 ml/(g_{cat}.hr.) at the feed molar composition of $\text{CH}_4:\text{CO}_2:\text{H}_2\text{O}:\text{N}_2 = 1.0:0.4:0.8:2.0$ to reach a syngas molar ratio of $\text{H}_2:\text{CO}$ equal to around 2.0. The temperature of the catalyst bed increased from the ambient temperature to 800 °C at a constant rate of 5 °C/min. Once the temperature reached the desired point, the catalyst sample was reduced for 2 hours under a flow of 20%:80% $\text{H}_2:\text{N}_2$ stream at a rate of 150 ml/min.

For the sake of comparison, the catalytic activity of a commercial steam reforming catalyst (10.2% Ni on MgAl_2O_4) was also evaluated.

3. Results and discussion

3.1. Catalyst characterization

Figure 2 depicts the XRD pattern of the as-prepared HT with Mg/Al molar ratio=1 which was synthesized according to the procedure mentioned before. As indicated, the pattern shows a Mg-Al HT like structure with the relevant peaks. The peaks at $2\theta^\circ$ around 12.4 and 24.15 are assigned to the (0 0 3) and (0 0 6) reflections respectively and can be used to calculate the basal spacing between the layers, i.e. d . The peak at $2\theta = 61.25$ is assigned to the (1 1 0) reflection and can be used to calculate the unit cell dimension, a , where $a = 2d_{110}$. The lattice parameter and basal plane spacing of the HT sample is listed in Table 1.

Table 1

Calculation of the lattice parameter and basal plane spacing of the hydrotalcite sample.

Mg/Al ratio	Nominal molar composition $x = \text{Al}/(\text{Al} + \text{Mg})$	(0 0 3) reflection ($2\theta^\circ$)	d (0 0 3) (Å)	(1 1 0) reflection ($2\theta^\circ$)	d (1 1 0) (Å)	a (Å)
1	0.50	12.43	7.11	61.42	1.508	3.016

Figure 3 shows the IR spectra of the dried samples synthesized with Mg/Al=1 at different ageing times. The results exhibit a typical broad band at about 3471 cm^{-1} , which is attributed to the stretching mode of hydrogen bonded hydroxyl groups from the brucite-like layers and interlayer water. The band at about 1623 cm^{-1} is H_2O bending vibration, while the bands localized around 1363 cm^{-1} could be attributed to Al–O and Al–OH vibrations, which confirm the presence of $\text{Al}(\text{OH})_3$ for all HT precursors structures. The low frequency region shows a band at about 560 cm^{-1} , which corresponds to the translation modes of hydroxy groups, influenced by Al^{3+} cations (Abello et al., 2005).

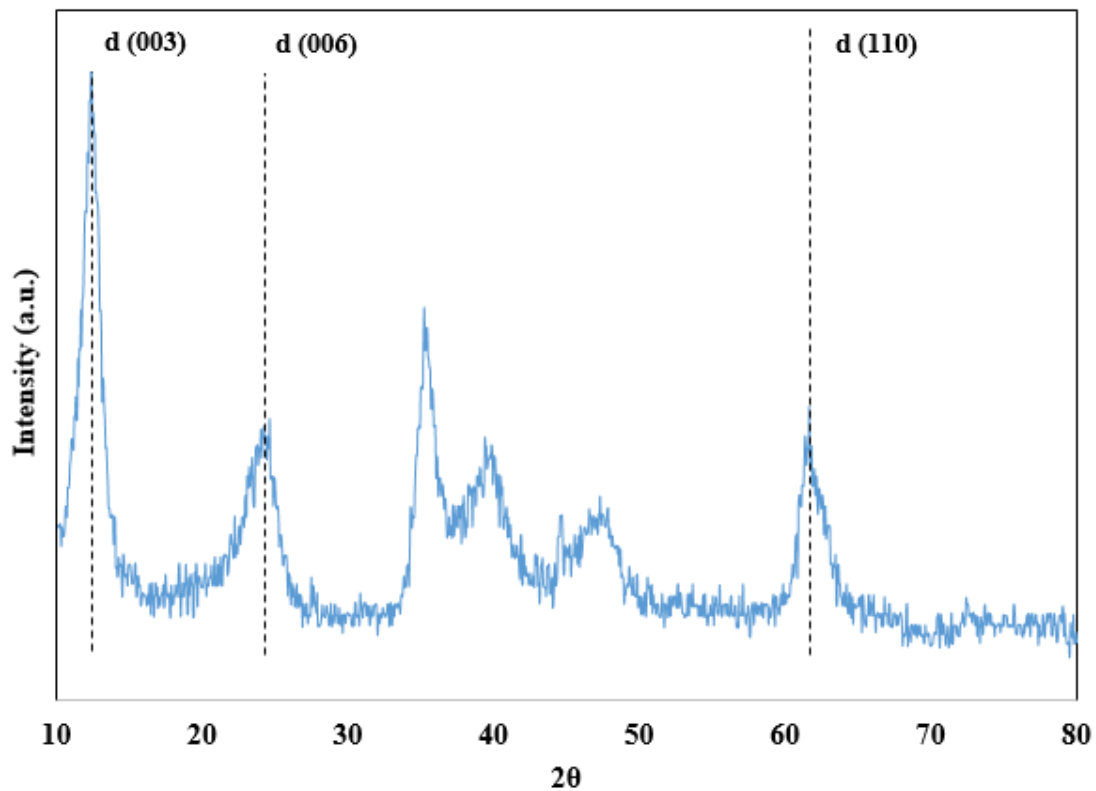


Figure 2

X-ray diffraction pattern of the as-prepared HT with Mg/Al=1.0.

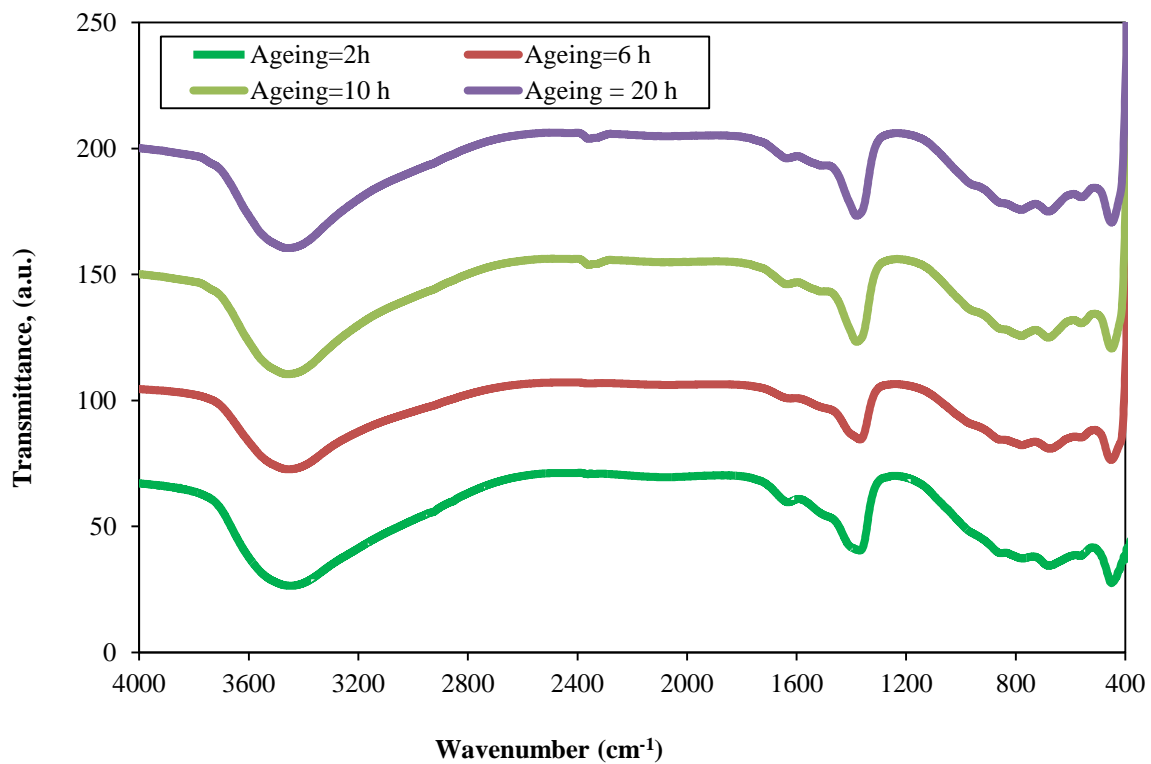


Figure 3

FTIR spectrum of the as-prepared HT sample with Mg/Al=1.

The effect of aging time on the surface area and textural properties of the Mg-Al HT samples aged for 2, 6, 10, and 20 hours and calcined for 2 hours at 700 °C was also investigated (see Table 2). This experiment implies that the sample aged for 6 hours has the highest surface area (slightly higher than the sample aged for 2 hours). In addition, the diagrams of the XRD experiments conducted on the samples aged for 2 and 6 hours show a similar pattern (which is not presented here) and confirm that there is no new transformation or significant growth for the samples aged for 4 hours or longer.

Table 2

Effect of aging time on the surface area and textural properties of the Mg-Al HT-like components with Mg/Al=1 calcined at 700 °C for 4 hours.

Ageing time (hr.)	Surface area (m ² /g)	Pore volume (ml/g)	Average pore size (4V/A) (nm)
2	247	0.7634	9.087
6	240	0.8944	11.37
10	176	0.8593	16.68
20	178	0.834	16.56

Figure 4 illustrates the XRD patterns of the Mg-Al hydrotalcite with Mg/Al=1 (aged for 6 hours) calcined at different temperatures of 500, 600, 700, and 800 °C. It is revealed that a dominant periclase phase is detected for all the samples and the trends of increasing temperature does not highly affect the cryptographic structure and the height of the peaks; finally, crystallite sizes are not changed significantly. Additionally, because of low calcination temperature, no MgAl₂O₄ spinel peaks are detected.

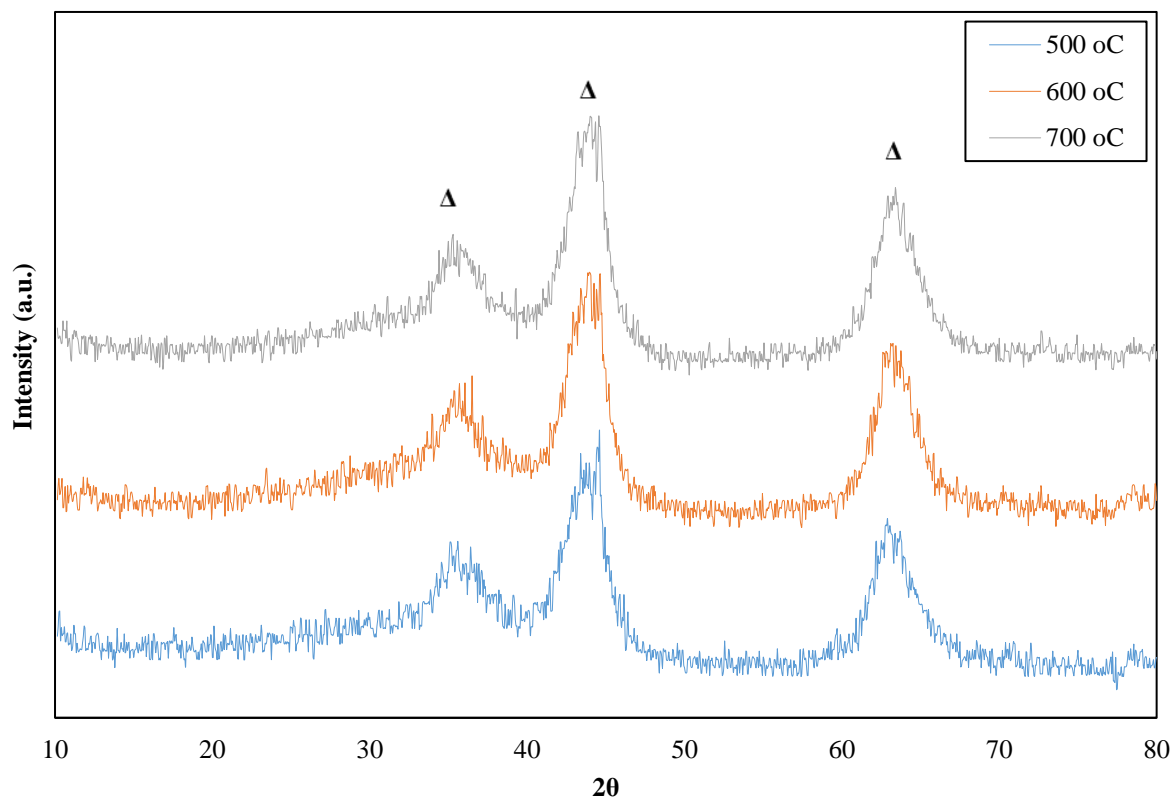


Figure 2

XRD patterns of the pre-calcined MgO-Al₂O₃ supports calcined at different temperatures.

The results of surface area, pore volume, and pore size distribution of the HT-like components calcined at different temperatures are presented in Table 3. As indicated, the samples which was calcined at 700 °C have the highest surface area, so 700 °C seems to be the most proper calcination temperature. It is expected that the highest nickel surface area and lowest nickel crystallite size can be obtained at 700 °C. The high surface area can be related to the precise pH and temperature control during the synthesis step.

Table 3

Variation in the surface area, pore volume, and pore size distribution of the Mg-Al HT-like components calcined at different temperatures (Mg/Al=1, aged for 2 hours).

Calcination temperature (°C)	Surface area (m ² /g)	Pore volume (ml/g)	Average pore size (nm)	Carrier crystallite size* (nm)
500	249	0.578	7.55	2.6
600	289	0.642	7.93	2.9
700	299	0.669	7.80	3.3
800	223	0.624	9.06	3.8

* The values in this column were obtained from the XRD experiments.

Figure 5 depicts the adsorption and desorption isotherm of the catalyst carriers calcined at different temperatures. This figure shows the type IV isotherm of all the calcined samples, according to the International Union of Pure and Applied Chemistry classification, which implies mesoporous structures with a high energy of adsorption. Moreover, the hysteresis loop is the type H3 attributed to slit-like pores. As represented in Figure 6 and in accordance with the values of average particle size obtained from the BJH method (Table 3), the pore size distribution curves for all the samples are sharp where their corresponding peaks are within 7-9 nm; moreover, the majority of the distribution curves are mostly located in the conventional mesoporous region, while a small part of the tail of the curves are outside that region.

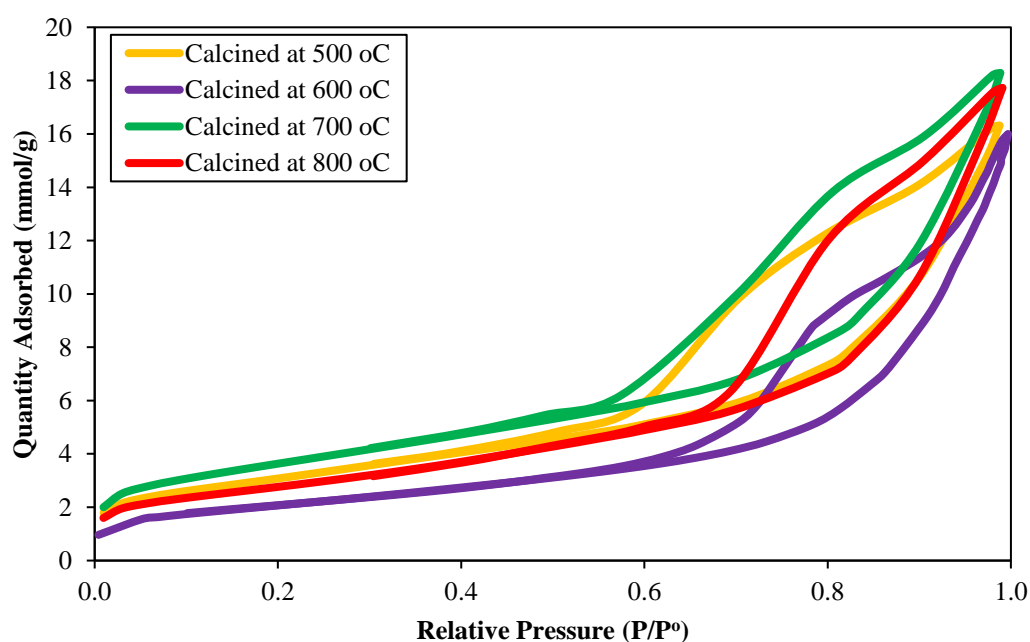


Figure 3

N₂ adsorption-desorption isotherms for the HT calcined at different temperatures.

According to Figure 7, the XRD pattern of the impregnated mixed oxide calcined at 700 °C confirms that, due to peak overlapping, it is hard to distinguish the peak of magnesium oxide from that of nickel oxide (NiO formed after the thermal decomposition of nickel nitrate during calcination). Therefore, the size of nickel oxide particles and subsequently nickel crystallite after in situ reduction inside the reactor could not be obtained using X-ray diffraction patterns.

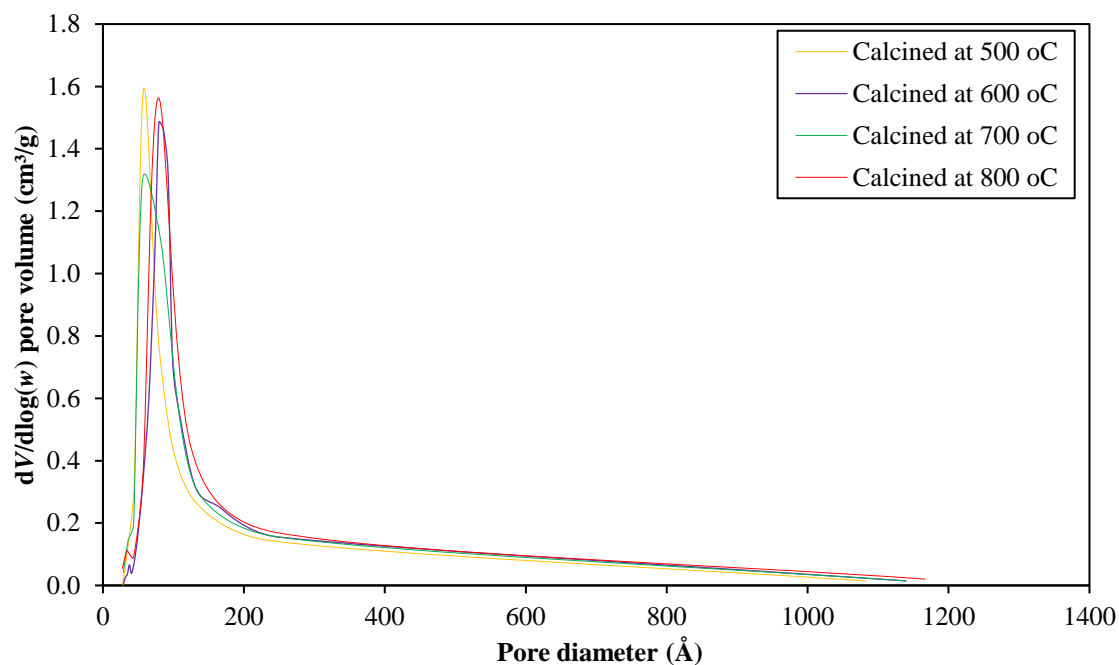


Figure 6

Pore size distribution of the HT samples calcined at different temperature.

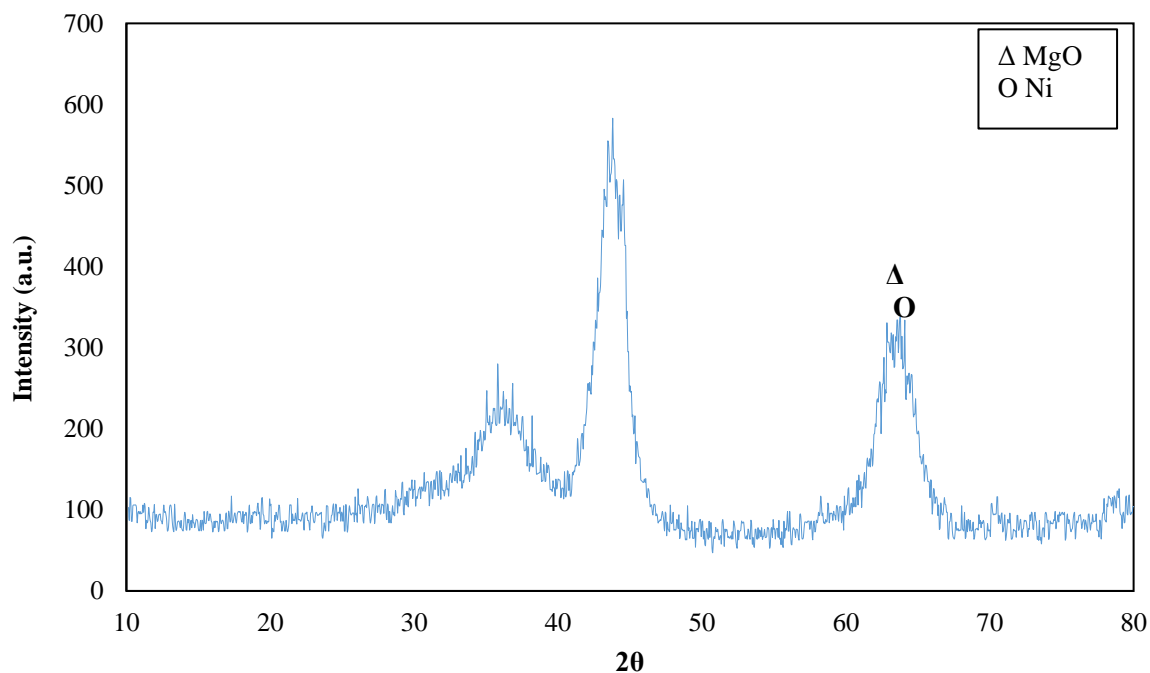


Figure 7

XRD patterns of 10% Ni-MgO-Al₂O₃ supports.

The temperature programmed reduction (TPR) profiles of the synthesized catalysts are represented in Figure 8; except for the sample calcined at 500 °C with a small and broad peak in the low temperature range, all the samples exhibit reduction peaks at rather high temperatures (600-800 °C with a small shoulder up to 850 °C), indicating a strong MST which could be remarkably favorable (Jabbour et al., 2016; Smoláková et al., 2015). It should be noted that the presence of such peaks at temperatures lower than 500 °C can be attributed to the reduction of nickel oxide particles weakly bound with the catalyst support or to the reduction of bulk nickel oxide. The disappearance of small peaks at low temperatures along with the change in the shape of TPR peaks can be explained by the fact that raising calcination temperature strengthens MSI more and more. According to the TPR profiles (Figure 8), it seems that the decomposition of the precursors at 700 °C provides the highest MSI, and as explained earlier, this implies that, as it is expected, the catalyst synthesized using this support has the highest activity and stability compared to the others. However, increasing the calcination temperature to more than 800 °C may likely shift the TPR profile to the left side of the profile obtained at 800 °C, and some inactive and irreducible nickel-alumina phase may form, which results in the decrease of the activity due to expanding nickel crystallite and reducing MSI (Koo et al., 2008).

As mentioned, the major area under the peaks observed for all the samples are in the region in which the catalyst samples are reducible below 800 °C, meaning that no limitation to the catalytic activity of the samples would be expected in CSDRM reaction at that temperature since almost all the dispersed nickel oxide nanoparticles can be reduced to the metallic form.

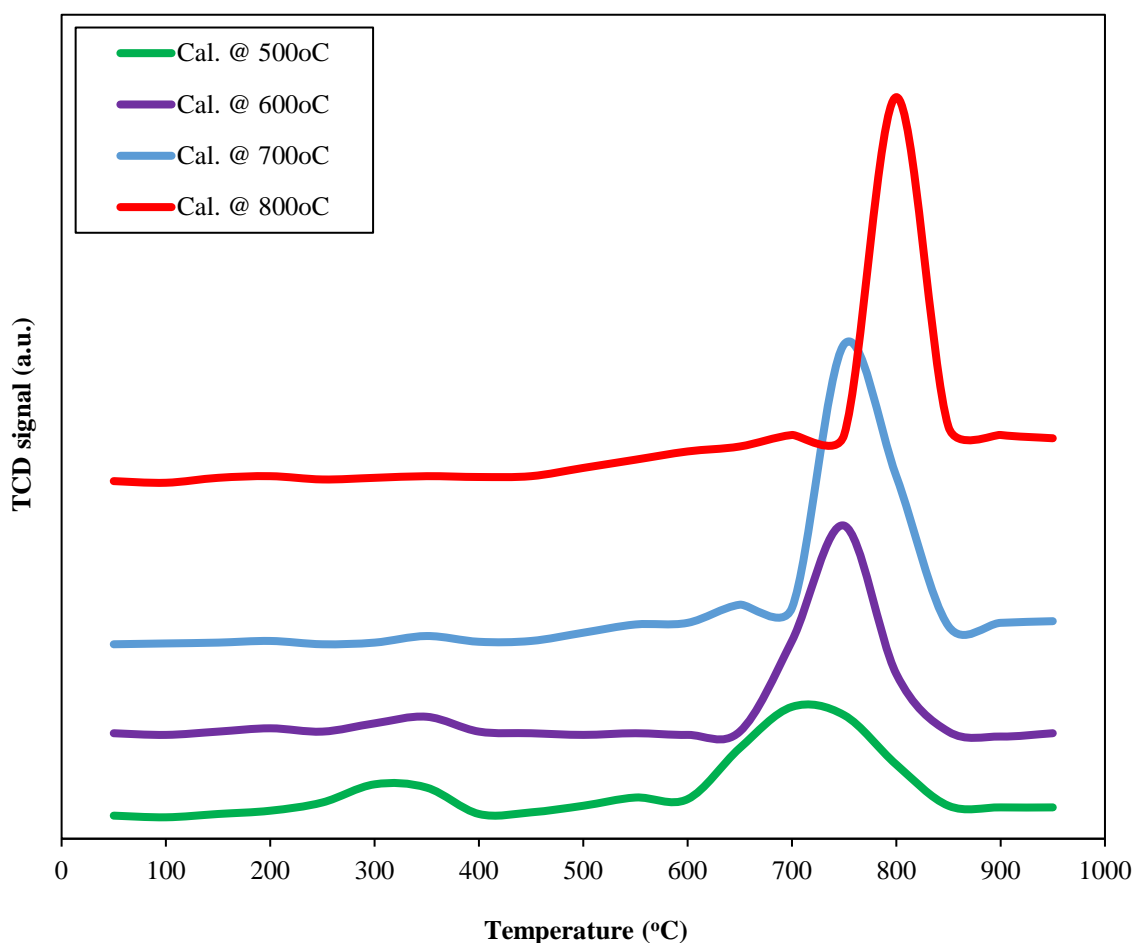


Figure 8

H₂-TPR profiles of the HT samples calcined at different temperatures.

The evaluation of H₂ chemisorption of the catalysts impregnated with nickel nitrate to obtain the same 10%Ni for all the samples reveals a trend similar to the variation of catalyst surface area with calcination temperature. It is not surprising to see that the dispersion and surface area of nickel of the samples are both substantially higher than those of the commercial catalyst sample (see Table 4). It is expected that the catalysts with a smaller nickel crystallite size and a higher nickel surface area have a higher activity to convert reactants. However, the stability of the catalyst during the long-term experiments should also be considered.

Table 4

Effect of calcination temperature of the HT on the surface area and chemisorption properties of the catalyst for 10%Ni-MgO-Al₂O₃.

Calcination temperature (°C)	Nickel content (wt.%)	Catalyst surface area (m ² /g)	Nickel dispersion (%)	Nickel surface area (m ² /g)	Average nickel crystallite size (nm)
500	9.85	122	25.02	16.41	4.04
600	9.89	146	34.42	22.66	2.94
700	9.95	167	37.75	25.01	2.68
800	10.12	101	20.01	13.48	5.06
Commercial catalyst	12.02	12	0.9	0.93	105.37

For the sake of studying the texture properties of the synthesized catalyst, the TEM image of the catalyst obtained from the precursor decomposed at 700 °C is displayed in Figure 9. It indicates a well-dispersed and nanostructure texture with some needles which may be attributed to aluminum oxide particles. The nickel crystallites are well dispersed inside the structure, and such sizes may explain the reason for the high catalytic activity of the catalysts.

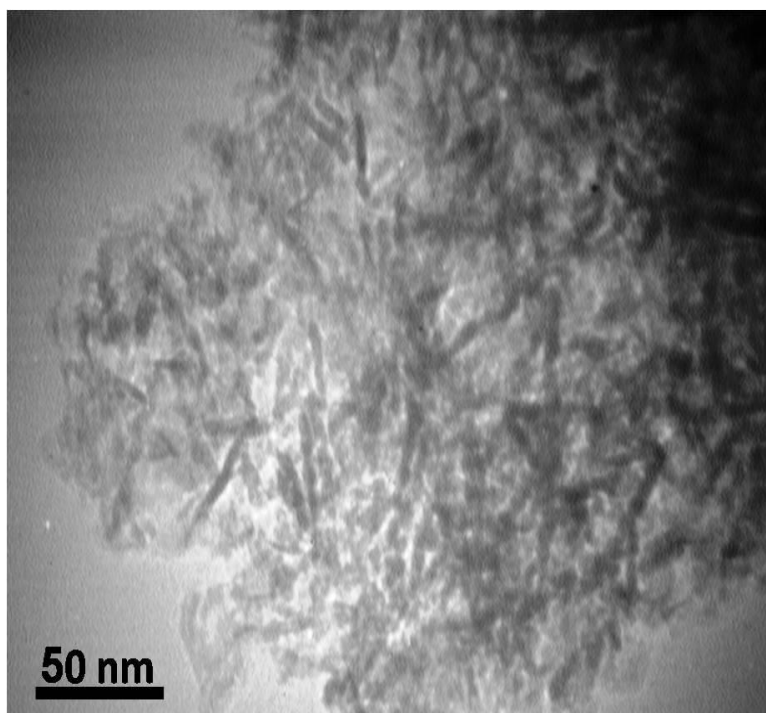


Figure 9

TEM image of the catalyst obtained from the precursor decomposed at 700 °C.

3.2. Reaction Results

In order to screen the catalyst activity to obtain a sample with the highest activity, the CSDRM reaction was carried out at 800 °C at a molar composition of CH₄:CO₂:H₂O:N₂=1.0:0.4:0.8:2.0 during a 36-hour run at a space velocity of 150,000 ml/g_{cat}.hr. The results of the catalyst activity testing demonstrate the high initial and final conversion (after 36 hours of catalyst testing) of CO₂ and CH₄ to H₂ and CO for all the samples with a slight difference between them; however, the sample decomposed at 700 °C displayed the highest CO₂ and CH₄ conversion, which is in accordance with the hydrogen chemisorption experiments (see Table 5). Since the high activity of all the samples arises from the high nickel surface area, the product composition are only a few percent far from equilibrium conditions, while, as expected, such a behavior is not observed for the commercial catalyst. More importantly, the excellent stability of the catalysts during the experiments may be as a result of either the enhanced basicity, which inhibits the deposition of coke, or slow nickel sintering due to high interaction between the catalyst carrier and nickel particles. The evolution of the composition of the reaction products in the effluent in the presence of the catalyst decomposed at 700 °C is depicted in Figure 10, which indicates a stable and highly active sample for the CSDRM reaction.

Table 5

Conversions and H₂:CO molar ratio over the catalysts synthesized at different temperatures (test duration=36 hrs) after CSDRM (CH₄:CO₂:H₂O:N₂= 1.0:0.4:0.8:2.0, T= 800 °C, gas hourly space velocity (GHSV)=150,000 hr.⁻¹, P= 9 psig). Initial values were obtained at time on stream (TOS)=1 hr. after the test started, and final values were obtained at TOS= 36 hrs.

HT calcination temperature (°C)	Initial CH ₄ conversion (%)	Final CH ₄ conversion (%)	Initial CO ₂ conversion (%)	Final CO ₂ conversion (%)	Initial H ₂ :CO	Final H ₂ :CO
500	91.9	91.3	72.6	72.4	2.04	2.04
600	93.0	92.5	75.0	74.4	2.03	2.03
700	93.7	93.4	75.6	75.2	2.03	2.03
800	91.2	90.6	71.3	70.7	2.05	2.05
Commercial catalyst	83.2	78.51	61.9	55.22	2.08	2.12

The results of the carbon content of the samples, obtained from the carbon elemental analyzer device, along with the corresponding CH₄ conversion values are illustrated in Figure 11. The results demonstrate the excellent coke resistance of the samples. It should be noted that the lowest carbon content is for the most active sample, but the other samples also contain a low carbon content. In general, the low carbon deposited on the catalysts may be because of either the enough number and strength of the basic sites, which can improve the adsorption of acidic CO₂ gas to supply the surface oxygen and suppress the coke deposition, or low nickel crystallite size (Koo et al., 2009).

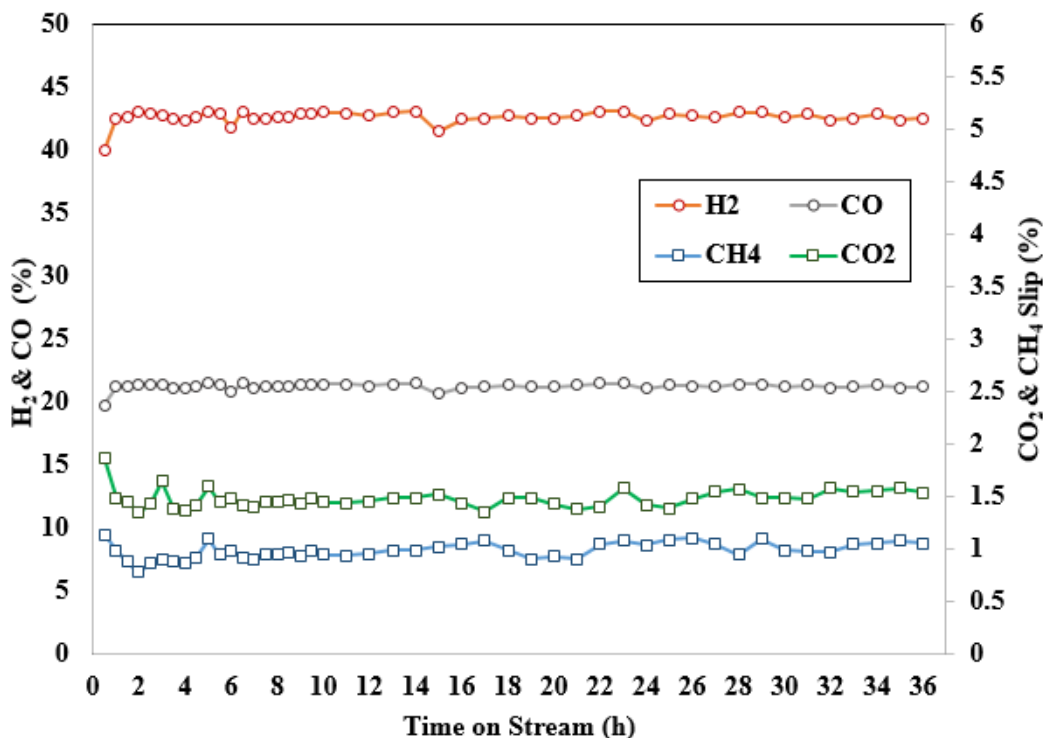


Figure 10

Evolution of CH₄, H₂, CO, and CO₂ with time (dry basis) over 10%Ni-MgO-Al₂O₃ (the sample was calcined at 700 °C) after 36 hours at 800 °C, GHSV=240,000 ml/g_{cat}.hr. and CH₄:CO₂:H₂O:N₂=1.0:0.4:0.8:2.0.

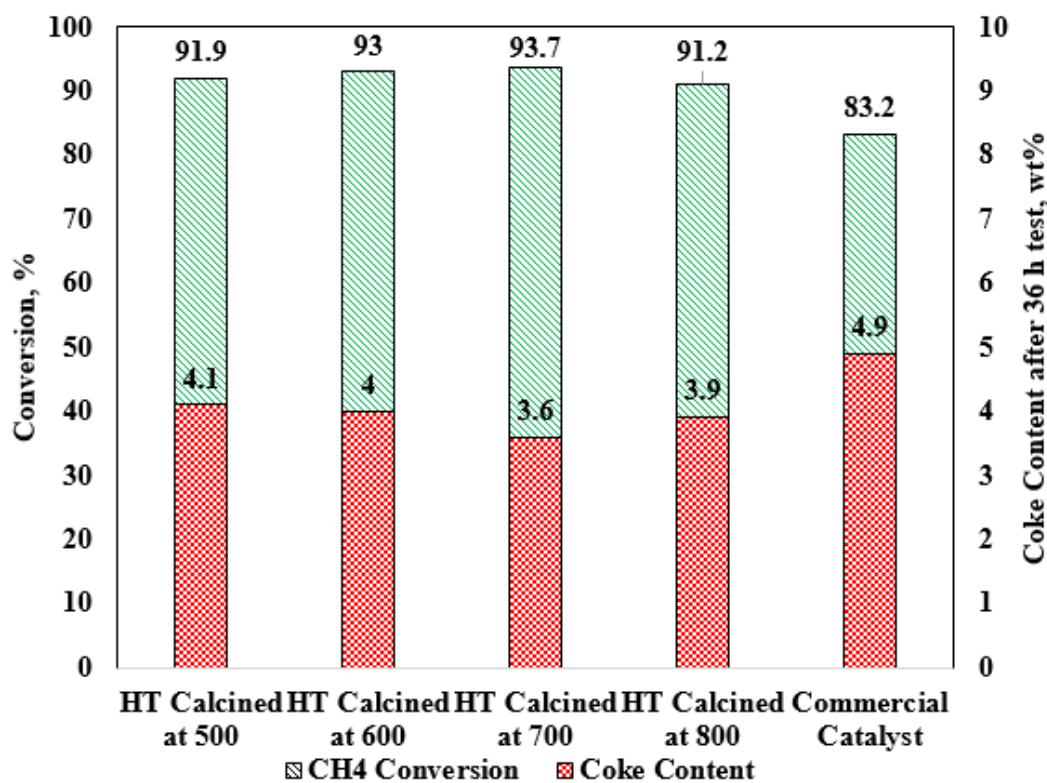


Figure 11

CH₄ conversion and coke content over 10%Ni-MgO-Al₂O₃ for various samples after 36 hours at 800 °C, GHSV=240,000 ml/g_{cat}.hr. and CH₄:CO₂:H₂O:N₂=1.0:0.4:0.8:2.0.

In the work of Jabbour et al., different nickel loadings and various reaction temperatures at two GHSV's were studied in the CSDRM (Jabbour et al., 2017). The highest GHSV used in their work was 138,000 ml/(g_{cat}.hr.), which is slightly less than the one in our contribution (GHSV=150,000 ml/(g_{cat}.hr.)). The duration of the catalyst activity test in both cases was nearly similar, and the temperature of the reaction in both works was 800 °C; pressure was almost atmospheric in both studies, and the feedstock molar composition was CH₄:CO₂:H₂O=1.0:0.4:0.8.

Table 6

Comparison of CH₄ and CO₂ conversions, H₂:CO molar ratio, and the coke content over the spent catalysts for the optimum catalyst synthesized in this study versus those used in the work of Jabbour et al. during the nearly same run duration (CH₄:CO₂:H₂O= 1:0.4:0.8, T= 800 °C, P= 1atm).

	Catalyst type	Initial CH ₄ conversion (%)	Initial CO ₂ conversion (%)	Final CH ₄ conversion (%)	Final CO ₂ conversion (%)	Initial H ₂ :CO	Final H ₂ :CO	Coke content (wt.%)
Jabbour et al.	Ni5%Al ₂ O ₃	57.0	51.0	59.0	54.0	2.12	2.17	9.00
	Ni7.5%Al ₂ O ₃	66.0	63.0	67.0	61.0	2.20	2.22	12.00
	Ni10%Al ₂ O ₃	81.0	79.0	82.0	77.0	2.27	2.33	19.00
	Ni5%Ca5%Al ₂ O ₃	64.0	58.0	65.0	58.0	2.09	2.05	4.00
	Ni5%Mg5%Al ₂ O ₃	79.0	73.0	80.0	74.0	2.10	2.10	3.00
Our study	Ni10%MgO.Al ₂ O ₃	93.7	75.6	93.4	75.2	2.03	2.03	3.60

As specified in Table 6, the initial and final conversions of both CH₄ and CO₂ are higher in this study in the optimum condition, i.e. a calcination temperature of 700 °C for the HT-derived catalyst carrier, compared to all the catalyst samples used in the work of Jabbour et.al, which confirms the higher activity of our sample at the beginning and at the end of the activity experiment. Furthermore, the coke content of the catalyst in this study is relatively lower than those in the work of Jabbour et.al, indicating the excellent resistance of our catalyst against coke formation compared to the catalysts used in the work of Jabbour et al. Nevertheless, a higher catalytic activity was achieved in our sample during the long-time run.

According to Jabbour et al., the adsorption-activated mechanisms for the dry reforming of methane (DRM), steam reforming of methane (SRM), and CSDRM are explained. As indicated, several activation elementary steps are distinguished for the CSDRM.

In Table 7, * stands for the adsorbed activated atoms; for example, O* means an adsorbed activated oxygen atom. According to the above mechanism, C* (adsorbed activated carbon) is responsible for the formation of the product (CO) as well as coke. It can be expected that catalyst carrier through enhancing the formation of adsorbed activated oxygen (O*) on the surface can inhibit the precipitation of carbon or its polymerization on the catalyst (Jabbour et al., 2017). In other words, it is necessary for the catalyst carrier to have a high basicity facilitating H₂O and CO₂ dissociation to inhibit or reduce the participation of C* to carbon polymerization phenomena which leads to coke formation. In mesoporous MgO-Al₂O₃ catalyst carriers, it is very important to obtain the strongest basic sites as well as the highest total basic density. It can be seen that the highest basicity is achieved at an HT calcination temperature of 700 °C,

so the highest rate of reduction in coke deposition is attained. In conclusion, it is desirable to have a trade-off between the surface area of the catalyst carrier to have a high initial activity and its basicity to preserve its activity over time.

Table 7

Adsorption-activated mechanisms for the main reactions in the CSDRM.

Reaction type	Mechanism
CH ₄ activation (I)	$\square\square_4 + 2* \rightarrow \square\square_3* + *$ $\square\square_3* + * \rightarrow \square\square_2* + \square*$ $\square\square_2* + * \rightarrow \square\square* + \square*$ $\square\square* + * \rightarrow \square* + \square*$
H ₂ O activation (II)	$\square_2\square + * \rightarrow \square_2 + \square*$
CO ₂ activation (III)	$\square\square_2 + * \rightarrow \square\square_2*$ $\square\square_2* + * \rightarrow \square\square* + \square*$ $\square\square* \rightarrow \square\square + *$
Surface reactions (IV)	$\square* + \square* \rightarrow \square\text{O} + 2*$ $\square\text{O}^* \rightarrow \square\text{O} + *$ $H^* + H^* \rightarrow H_2 + 2*$

4. Conclusions

Several nickel-based catalysts supported on mesoporous MgO-Al₂O₃ (10%Ni) are derived from Mg-Al hydrotalcite-like structure with Mg/Al=1. The HT-like components are synthesized at a carefully controlled pH of 10 to give a homogeneous texture with a high surface area. The hydrotalcite-like precursor is then calcined at different calcination temperatures in the range of 500-800 °C. Ultimately, 10% nickel is impregnated on all the calcined samples. The results of catalyst performance testing for the CSDRM reaction at 800 °C during the long-term 36-hour run (feed stock composition: CH₄:CO₂:H₂O=1.0:0.4:0.8) at GHSV=150,000 ml/g_{cat}.hr. indicate that the sample prepared from the carrier calcined at 700 °C exhibits the highest nickel surface area (25.01 m²/g) and the lowest nickel crystallite size (2.68 nm).; also, it has the highest activity (an initial conversion of 93.7% and 75.6% for methane and CO₂ respectively) and stability (a final conversion of 93.4% and 75.2% for methane and CO₂ respectively) with excellent resistance to coke formation. The high resistance to coke formation can be attributed to the high strength of the basic sites formed in the catalyst carrier during the HT-like component calcination at 700 °C. Finally, the results of the catalyst testing experiment indicate a significant higher activity and resistance to coke formation compared to the commercial reforming catalyst.

Nomenclature

Abbreviations	
CSDRM	Combined steam and dry reforming of methane
DRM	Dry reforming of methane
FT-IR	Fourier-transform infrared spectroscopy
FWHM	Full width at half maximum
HT	Hydrotalcite
SRM	Steam reforming of methane

TPR	Temperature programmed reduction
Latin Symbols	
a_{Ni}	Nickel atom cross section, 6.49×10^{-20} [m ² /Ni atoms]
d	Crystalline size [nm]
d_{av}	Average nickel crystallite diameter [nm]
D_m	Nickel dispersion [%]
ΔH_{298}^0	Molar enthalpy change of reaction at 298 K, [kJ/mol]
$F_{CH_4,in}$	Molar flowrate of CH ₄ at the reactor inlet [gmol/min]
$F_{CH_4,out}$	Molar flowrate of CH ₄ at the reactor outlet [gmol/min]
$F_{CO_2,in}$	Molar flowrate of CO ₂ at the reactor inlet [gmol/min]
$F_{CO_2,out}$	Molar flowrate of CO ₂ at the reactor outlet [gmol/min]
GHSV	Gas hourly space velocity, [ml/(g _{cat} .hr.)]
K	Dimensionless shape factor in Scherrer equation, (Assumed here to be 0.9)
N_{Av}	Avogadro number, 6.023×10^{23} [atoms/gmol]
N.SA	Nickel surface area, [m ² /g]
S.F.	Stoichiometric factor, [unitless, for hydrogen chemisorption, H/Ni=1]
V_{chem}	Hydrogen chemisorbed volume [mol/g]
Greek Symbols	
β	Line broadening at half the maximum intensity [Radian]
λ	X-ray wavelength [Å]
ρ	Nickel density [g/cm ³]
θ	Scattering angle (half of the Bragg angle) [degree]

Acknowledgements

This work as a joint research between the Chemical Engineering Department of IUT and the R&D Department of KhTD Company was supported and funded by KhTD Company (grant number: 2016-940401).

References

- Abelló, S., Medina, F., Tichit, D., Pérez-Ramírez, J., Groen, J. C., Sueiras, J. E., Salagre, P., and Cesteros, Y., Aldol Condensations over Reconstructed Mg–Al Hydrotalcites: Structure–activity Relationships Related to the Rehydration Method, *Chemistry-A European Journal*, Vol. 11, No. 2, p. 728-739, 2005.
- Arizaga, G. G. C., Satyanarayana, K. G., and Wypych, F., Layered Hydroxide Salts: Synthesis, Properties and Potential Applications, *Solid State Ionics*, Vol. 178, No. 15, p. 1143-1162, 2007.
- Bae, J. W., Kim, A. R., Baek, S.-C., and Jun, K. W., The Role of CeO₂–ZrO₂ Distribution on the Ni/MgAl₂O₄ Catalyst during the Combined Steam and CO₂ Reforming of Methane, *Reaction Kinetics, Mechanisms and Catalysis*, Vol. 104, No. 2, p. 377-388, 2011.
- Boukha, Z., Fitian, L., López-Haro, M., Mora, M., Ruiz, J. R., Jiménez-Sanchidrián, C., Blanco, G., Calvino, J. J., Cifredo, G. A., Trasobares, and S., Bernal, S., Influence of the Calcination

- Temperature on the Nanostructural Properties, Surface Basicity, and Catalytic Behavior of Alumina-supported Lanthana Samples, *Journal of Catalysis*, Vol. 272, No. 1, p. 121-130, 2010.
- Cavani, F., Trifirò, F., and Vaccari, A., Hydrotalcite-type Anionic Clays: Preparation, Properties and Applications, *Catalysis Today*, Vol. 11, No. 2, p. 173-301, 1991.
- Christensen, K. O., Chen, D., Lødeng, R., and Holmen, A., Effect of Supports and Ni Crystal Size on Carbon Formation and Sintering During Steam Methane Reforming, *Applied Catalysis A: General*, Vol. 314, No. 1, p. 9-22, 2006.
- Cullity, B. D. and Stock, S. R., *Elements of X-Ray Diffraction: Pearson New International Edition*. Pearson Education Limited, 2013.
- Danilova, M. M., Fedorova, Z. A., Kuzmin, V. A., Zaikovskii, V. I., Porsin, A. V., and Krieger, T. A., Combined Steam and Carbon Dioxide Reforming of Methane over Porous Nickel-based Catalysts, *Catalysis Science and Technology*, Vol. 5, No. 5, p. 2761-2768, 2015.
- Daza, C. E., Moreno, S., and Molina, R., Ce-promoted Catalyst from Hydrotalcites for CO₂ Reforming of Methane: Calcination Temperature Effect, *Química Nova*, Vol. 35, No., p. 1325-1328, 2012.
- Duan, X. and Evans, D. G., *Layered Double Hydroxides*, Springer Science and Business Media: Vol. 119, 2006.
- Fonseca, A. and Assaf, E. M., Production of the Hydrogen by Methane Steam Reforming over Nickel Catalysts Prepared from Hydrotalcite Precursors, *Journal of Power Sources*, Vol. 142, No. 1-2, p. 154-159, 2005.
- Huang, B., Li, X., Ji, S., Lang, B., and Habimana, F., Li, C., Effect of MgO Promoter on Ni-based SBA-15 Catalysts for Combined Steam and Carbon Dioxide Reforming of Methane, *Journal of Natural Gas Chemistry*, Vol. 17, No. 3, p. 225-231, 2008.
- Itkulova, S.S; Nurmakanov, Y.Y., Kussanova, S.K., and Boleubayev, Y.A., Production of a Hydrogen-enriched Syngas by Combined CO₂-steam Reforming of Methane over Co-based Catalysts Supported on Alumina Modified with Zirconia, *Catalysis Today*, Vol. 299 No. 1, p. 272-279, 2018.
- Jabbour, K., El Hassan, N., Davidson, A., Casale, S., and Massiani, P., Factors Affecting the Long-Term Stability of Mesoporous Nickel-based Catalysts in Combined Steam and Dry Reforming of Methane, *Catalysis Science and Technology*, Vol. 6, No. 12, p. 4616-4631, 2016.
- Jabbour, K., Kaydouh, M. N., El Hassan, N., El Zakhem, H., Casale, S., Massiani, P., and Davidson, A., Compared Activity and Stability of Three Ni-silica Catalysts for Methane Bi- and Dry Reforming, *Mediterranean Gas and Oil International Conference, Medgo 2015, Conference Proceedings*, Vol., No., p. 2-5, 2015.
- Jabbour, K., Massiani, P., Davidson, A., Casale, S., and El Hassan, N., Ordered Mesoporous One-pot Synthesized Ni-Mg(Ca)-Al₂O₃ as Effective and Remarkably Stable Catalysts for Combined Steam and Dry Reforming of Methane (CSDRM), *Applied Catalysis B: Environmental*, Vol. 201, No., p. 527-542, 2017.
- Koo, K. Y., Lee, S. H., Jung, U. H., Roh, H. S., and Yoon, W. L., Syngas Production via Combined Steam and Carbon Dioxide Reforming of Methane over Ni-Ce/MgAl₂O₄ Catalysts with Enhanced Coke Resistance, *Fuel Processing Technology*, Vol. 119, No., p. 151-157, 2014.

- Koo, K. Y., Roh, H.-S., Jung, U. H., Seo, D. J., Seo, Y.-S., and Yoon, W. L., Combined H₂O and CO₂ Reforming of CH₄ over Nano-sized Ni/MgO-Al₂O₃ Catalysts for Synthesis Gas Production for Gas to Liquid (GTL): Effect of Mg/Al Mixed Ratio on Coke Formation, *Catalysis Today*, Vol. 146, No. 1, p. 166-171, 2009.
- Koo, K. Y., Roh, H.-S., Jung, U. H., and Yoon, W. L., Combined H₂O And CO₂ Reforming of CH₄ over Ce-promoted Ni/Al₂O₃ Catalyst for Gas to Liquid (GTL) Process: Enhancement of Ni-CeO₂ Interaction, *Catalysis Today*, Vol. 185, No. 1, p. 126-130, 2012.
- Koo, K. Y., Roh, H.-S., Seo, Y. T., Seo, D. J., Yoon, W. L., and Bin Park, S., A Highly Effective and Stable Nano-sized Ni/MgO-Al₂O₃ Catalyst for Gas to Liquids (GTL) Process, *International Journal of Hydrogen Energy*, Vol. 33, No. 8, p. 2036-2043, 2008.
- Koo, K. Y., Roh, H.-S., Seo, Y. T., Seo, D. J., Yoon, W. L., and Park, S. B., Coke Study on MgO-promoted Ni/Al₂O₃ Catalyst in Combined H₂O and CO₂ Reforming of Methane for Gas to Liquid (GTL) Process, *Applied Catalysis A: General*, Vol. 340, No. 2, p. 183-190, 2008.
- Marquevich, M., Farriol, X., Medina, F., and Montané, D., Steam Reforming of Sunflower Oil over Ni/Al Catalysts Prepared from Hydrotalcite-like Materials, *Catalysis Letters*, Vol. 85, No. 1, p. 41-48, 2003.
- Mehr, J. Y., Jozani, K. J., Pour, A. N., and Zamani, Y., Influence of MgO in the CO₂-steam Reforming of Methane to Syngas by NiO/MgO/ and Alpha-Al₂O₃ Catalyst, *Reaction Kinetics and Catalysis Letters*, Vol. 75, No. 2, p. 267-273, 2002.
- Olah, G. A., Goeppert, A., Czaun, M., Mathew, T., May, R. B., and Prakash, G. S., Single Step Bi-reforming and Oxidative Bi-reforming of Methane (Natural Gas) with Steam and Carbon Dioxide to Metgas (CO-2H₂) for Methanol Synthesis: Self-sufficient Effective and Exclusive Oxygenation of Methane to Methanol with Oxygen, *Journal of The American Chemical Society*, Vol. 137, No. 27, p. 8720-8729, 2015.
- Olah, G. A., Goeppert, A., Czaun, M., and Prakash, G. S., Bi-reforming of Methane from any Source with Steam and Carbon Dioxide Exclusively to Metgas (CO-2H₂) for Methanol and Hydrocarbon Synthesis, *Journal of The American Chemical Society*, Vol. 135, No. 2, p. 648-650, 2012.
- Olah, G. A., Goeppert, A., and Prakash, G. K. S., *Beyond Oil and Gas: The Methanol Economy*, Wiley, 2011.
- Park, J. E., Koo, K. Y., Jung, U. H., Lee, J. H., Roh, H.-S., and Yoon, W. L., Syngas Production by Combined Steam and CO₂ Reforming of Coke Oven Gas over Highly Sinter-stable La-promoted Ni/MgAl₂O₄ Catalyst, *International Journal of Hydrogen Energy*, Vol. 40, No. 40, p. 13909-13917, 2015.
- Ramasamy, K. K., Gray, M., Job, H., Santosa, D., Li, X. S., Devaraj, A., Karkamkar, A., and Wang, Y., Role of Calcination Temperature on the Hydrotalcite Derived MgO-Al₂O₃ in Converting Ethanol to Butanol, *Topics in Catalysis*, Vol. 59, No. 1, p. 46-54, 2016.
- Roh, H.-S., Koo, K. Y., Jeong, J. H., Seo, Y. T., Seo, D. J., Seo, Y.S., Yoon, W. L., and Park, S. B., Combined Reforming of Methane over Supported Ni Catalysts, *Catalysis Letters*, Vol. 117, No. 1, p. 85-90, 2007.
- Roh, H.-S., Koo, K. Y., Joshi, U. D., and Yoon, W. L., Combined H₂O and CO₂ Reforming of Methane over Ni-Ce-ZrO₂ Catalysts for Gas to Liquids (GTL), *Catalysis Letters*, Vol. 125, No. 3, p. 283-288, 2008.

- Roh, H.-S., Koo, K. Y., and Yoon, W. L., Combined Reforming of Methane over Co-precipitated Ni–CeO₂, Ni–ZrO₂, and Ni–Ce_{0.8}Zr_{0.2}O₂ Catalysts to Produce Synthesis Gas for Gas to Liquid (GTL) Process, *Catalysis Today*, Vol. 146, No. 1–2, p. 71-75, 2009.
- Rong Kim, A., Yong Lee, H., Min Cho. Jae, Hwan C.W., and Wook Bae, J., Ni/M–Al₂O₃ (M=Sm, Ce or Mg) for Combined Steam and CO₂ Reforming of CH₄ from Coke Oven Gas, *Journal of CO₂ Utilization*, Vol. 21, p. 211-218, 2017.
- Rostrup-Nielsen, J. R., Sehested, J., and Nørskov, J. K., Hydrogen and Synthesis Gas by Steam and CO₂ Reforming, *Advances in Catalysis*, Academic Press, Vol. 47, p. 65-139, 2002
- Rostrup-Nielsen, J. and Christiansen, L. J., *Concepts in Syngas Manufacture*, Imperial College Press., 2011.
- Sato, T., Kato, K., Endo, T., and Shimada, M., Preparation and Chemical Properties of Magnesium Aluminum Oxide Solid Solutions, *Reactivity of Solids*, Vol. 2, No. 3, p. 253-260, 1986.
- Schulze, K. Ni/Mg/Al Catalysts Derived from Hydrotalcite-type Precursors for the Partial Oxidation of Propane, *Universität Duisburg-essen, Fakultät Für Chemie*, 2001.
- Sehested, J., Gelten, J. A., and Helveg, S., Sintering of Nickel Catalysts: Effects of Time, Atmosphere, Temperature, Nickel-carrier Interactions, and Dopants, *Applied Catalysis A: General*, Vol. 309, No. 2, p. 237-246, 2006.
- Seo, J. G., Youn, M. H., Chung, J. S., and Song, I. K., Effect of Calcination Temperature of Mesoporous Nickel–Alumina Catalysts on their Catalytic Performance in Hydrogen Production by Steam Reforming of Liquefied Natural Gas (LNG), *Journal of Industrial and Engineering Chemistry*, Vol. 16, No. 5, p. 795-799, 2010.
- Siang, T.J., Pham, T.L.M., Cuong, N.V., and Phoung, P.T.T., Combined Steam and CO₂ Reforming of Methane for Syngas Production over Carbon-resistant Boron-promoted Ni/SBA-15 Catalysts, *Microporous and Mesoporous Materials*, Vol. 262, No. 15, p. 122-132, 2018.
- Smoláková, L., Kout, M., Koudelková, E., and Čapek, L., Effect of Calcination Temperature on the Structure and Catalytic Performance of The Ni/Al₂O₃ and Ni–Ce/Al₂O₃ Catalysts in Oxidative Dehydrogenation of Ethane, *Industrial & Engineering Chemistry Research*, Vol. 54, No. 51, p. 12730-12740, 2015.
- Son, I. H., Lee, S. J., Soon, A., Roh, H.S., and Lee, H., Steam Treatment on Ni/Γ–Al₂O₃ for Enhanced Carbon Resistance in Combined Steam and Carbon Dioxide Reforming of Methane, *Applied Catalysis B: Environmental*, Vol. 134, No., p. 103-109, 2013.
- Song, X. and Guo, Z., Technologies for Direct Production of Flexible H₂/CO Synthesis Gas, *Energy Conversion and Management*, Vol. 47, No. 5, p. 560-569, 2006.
- Tan, M., Wang, X., Wang, X., Zou, X., Ding, W., and Lu, X., Influence of Calcination Temperature on Textural and Structural Properties, Reducibility, and Catalytic Behavior of Mesoporous Γ–Alumina-supported Ni–Mg Oxides by One-pot Template-free Route, *Journal of Catalysis*, Vol. 329, No., p. 151-166, 2015.
- Xu, Z. P., Zhang, J., Adebajo, M. O., Zhang, H., and Zhou, C., Catalytic Applications of Layered Double Hydroxides and Derivatives, *Applied Clay Science*, Vol. 53, No. 2, p. 139-150, 2011.

- Yaakob, Z., Bshish, A., Ebshish, A., Tasirin, S., and Alhasan, F., Hydrogen Production by Steam Reforming of Ethanol over Nickel Catalysts Supported on Sol Gel Made Alumina: Influence of Calcination Temperature on Supports, *Materials*, Vol. 6, No. 6, p. 2229, 2013.
- Yang, Y., Liu, J., Shen, W., Li, J., and Chein, I.L., High-efficiency Utilization of CO₂ in the Methanol Production by a Novel Parallel-series System Combining Steam and Dry Methane Reforming, *Energy*, Vol. 158, No. 1, p. 820-829, 2018.
- Zhang, S., Muratsugu, S., Ishiguro, N., and Tada, M., Ceria-doped Ni/SBA-16 Catalysts for Dry Reforming of Methane, *ACS Catalysis*, Vol. 3, No. 8, p. 1855-1864, 2013.